



Graphene/silicon nanocomposite anode with enhanced electrochemical stability for lithium-ion battery applications



F. Maroni ^a, R. Raccichini ^b, A. Birrozzzi ^a, G. Carbonari ^a, R. Tossici ^a, F. Croce ^c, R. Marassi ^a, F. Nobili ^{a,*}

^a School of Science and Technology, Chemistry Division, University of Camerino, Via S. Agostino, 1, I-62032 Camerino, MC, Italy

^b Institute of Physical Chemistry, University of Muenster, Corrensstrasse 28/30, 48149 Muenster, Germany

^c Dipartimento di Farmacia, Università "G. D'Annunzio" Chieti-Pescara, Via dei Vestini 31, I-66100 Chieti, Italy

HIGHLIGHTS

- A high-capacity and high-stability graphene/silicon nanocomposite anode is prepared.
- Graphene oxide functionalization enhances silicon dispersion.
- High-molecular weight polyacrylic acid is used as green binder.
- Li–Si alloying phase transitions are characterized.
- Vinylene carbonate stabilizes interfacial properties.

ARTICLE INFO

Article history:

Received 27 April 2014

Received in revised form

28 June 2014

Accepted 9 July 2014

Available online 21 July 2014

Keywords:

Li-ion batteries

Nanocomposite material

Anode

Silicon

Graphene

Green binder

ABSTRACT

A graphene/silicon nanocomposite has been synthesized, characterized and tested as anode active material for lithium-ion batteries. A morphologically stable composite has been obtained by dispersing silicon nanoparticles in graphene oxide, previously functionalized with low-molecular weight polyacrylic acid, in eco-friendly, low-cost solvent such as ethylene glycol. The use of functionalized graphene oxide as substrate for the dispersion avoids the aggregation of silicon particles during the synthesis and decreases the detrimental effect of graphene layers re-stacking. Microwave irradiation of the suspension, inducing reduction of graphene oxide, and the following thermal annealing of the solid powder obtained by filtration, yield a graphene/silicon composite material with optimized morphology and properties.

Composite anodes, prepared with high-molecular weight polyacrylic acid as green binder, exhibited high and stable reversible capacity values, of the order of 1000 mAh g⁻¹, when cycled using vinylene carbonate as electrolyte additive. After 100 cycles at a current of 500 mA g⁻¹, the anode showed a discharge capacity retention of about 80%. The mechanism of reversible lithium uptake is described in terms of Li–Si alloying/dealloying reaction. Comparison of the impedance responses of cells tested in electrolytes with or without vinylene carbonate confirms the beneficial effects of the additive in stabilizing the composite anode.

© 2014 Elsevier B.V. All rights reserved.

1. Introduction

Since the early research and the subsequent introduction into the global market [1,2], Li-ion batteries have become one of the most promising electrical energy storage devices [3,4]. Over the years a vast research effort has been devoted to the improvement of the performances and reliability of the original Li-ion battery,

particularly on cathode and electrolyte sides [5–8]. On the anode side, carbonaceous active materials have consistently been the preferential choice [9,10]. Among them, graphite has been the most widely used in commercial applications because of the stability of the electrode/electrolyte interphase, the low and flat operating voltage, and the relatively high specific capacity of 372 mAh g⁻¹ [11,12]. However, anode materials alternative to graphite have been recently developed, with the aims of enhancing safety and increasing stored energy. Safety has been pursued developing materials, such as titanium oxide TiO₂ or lithium titanate Li₄Ti₅O₁₂, that operate far from the lithium deposition potential [13,14]. On

* Corresponding author. Tel.: +39 0737 402210; fax: +39 0737 402296.

E-mail addresses: francesco.nobili@unicam.it, nobilif@gmail.com (F. Nobili).

the other side in the attempt to increase specific energy, the use of materials able to reversibly exchange higher amounts of lithium has also been proposed, as is the case of graphene or alloy-based anodes [15,16].

In this context, silicon, one of the most abundant and cheap elements present on Earth crust, has been taken into account as candidate anode material [17] because of its high theoretical capacity of 4200 mAh g⁻¹, corresponding to the stoichiometry in Eq. (1).



Phase diagrams at elevated temperature predict formation of various compounds such as Li₁₂Si₇, Li₁₃Si₄, Li₇Si₃ prior of Li₂₂Si₅ [17]. However, the possible formation of Li₂₂Si₅ at room temperature is strongly questioned because of kinetic limitations and amorphization during cycling [18]. As a consequence, the end-member of lithium–silicon alloying processes has been identified as a crystalline Li₁₅Si₄ phase, with a theoretical capacity of 3579 mAh g⁻¹. Formation of this crystalline phase depends on the anodic cut-off potential and, more generally, on the cycling history of the electrode. Despite the high capacity, silicon electrodes suffer from serious drawbacks mostly related to the extremely high volume changes, up to 300%, that accompany the Li–Si alloying processes. This causes cracking and pulverization of the electrodes with subsequent loss of electric contact between active material and current collector [19–21]. In addition, the cracking of active material grains may expose new anode surface to electrolyte and induce formation of fresh solid electrolyte interphase (SEI), with subsequently low coulombic efficiency and increased electrode resistance [20]. Many efforts have been made in order to mitigate these effects. For instance, use of optimized morphologies, like those provided by silicon nanowires [22] or silicon nanoparticles synthesized by chemical vapor deposition [23], has been reported together with the use of different carbonaceous materials, such as Si-containing electrospun carbon nanotubes [24] or core–shell structures [25], to form composite electrodes in which the carbon matrix acts as a buffer that accommodates the Li–Si alloys volume variations. Graphene has recently been proposed as one of the best candidate matrix for composite anodes because of its open porous structure, that plays a ‘flexible confinement function’ for tolerating volume changes and gives a great mechanical strength to the composite. Its high surface specific area, in addition, favor storage of a high amount of Si nanoparticles by surface bonding, with an excellent electronic contact that enhances the electrode conductivity [26–30]. A second strategy used to limit the volume changes is the optimization of binder. The commonly used PolyVinylidene Fluoride (PVDF) interacts with Si nanoparticles via weak Van Der Waals forces that are not sufficiently strong for keeping the particles together and, hence, for stabilizing the electrode morphology [31]. Recently, high-molecular weight PolyAcrylic Acid (PAA) has been proposed as an alternative to PVDF, because of its high content of carboxylic groups that may strongly interact with the active material surface and current collector. In addition, PAA binder is much less prone than PVDF to swelling, promising a general improvement of the morphological stability. Finally, its solubility in non-toxic solvents as water or ethanol allows to decrease the costs and the environmental impact of the electrode processing [31,32].

In this context, this paper describes a novel synthetic route for a graphene/silicon nanocomposite starting from graphene oxide, low-molecular weight PAA and Si nanoparticles. PAA is used to functionalize graphene oxide. This limits its tendency to aggregate and enhances the dispersion of Si nanoparticles. The material obtained after microwave irradiation and thermal annealing exploits

the advantages of PAA-functionalized graphene as a wrapping, flexible buffering matrix for Si. Physical and chemical characterizations of the composite are carried out, and its performances as lithium-ion anode material are evaluated.

2. Experimental

2.1. Synthesis of silicon/reduced graphene oxide nanocomposite (Si/RGO)

The synthetic route for preparation of silicon/reduced graphene oxide nanocomposite (Si/RGO) is schematized in Fig. 1. 0.5 g of commercial graphene oxide (GO) powder (NanoInnova), were initially dispersed in 90 ml of ethylene glycol (Sigma–Aldrich Reagentplus, ≥99%) by bath sonication for 2 h. Subsequently, 2 g of low-molecular weight PAA powder (Sigma Aldrich, mw = 1800) were added to the suspension in order to promote the reaction of its carboxylic groups with the GO epoxy and hydroxyl moieties [33], resulting in PAA-functionalized graphene oxide (PAA-GO) [34]. The functionalization enhances the interlayer distances between graphene oxide planes and weakens the restacking tendency of graphene sheets.

After 1 h of further sonication, 0.1 g of commercial Si nanoparticles (~50 nm, Alfa Aesar), previously air-exposed to form a very thin superficial SiO_x layer, that favors silicon dispersion in polar solvent [35], were added to the suspension of PAA-GO.

Further 2 h of sonication enabled Si dispersion into the 3D-nanovoid structure of PAA-GO. The suspension was then placed into a modified domestic microwave oven and irradiated for 20 min under a medium power of 540 W. In this first reduction step, the PAA-GO matrix is partially reduced [36], while homogeneously dispersed silicon nanoparticles are anchored between the expanded sheets of the partially reduced PAA-GO [37]. The suspension was then vacuum filtered using a Fluoropore™ PTFE filter membrane and washed with ethanol in order to remove any possible excess of un-dispersed silicon not trapped into the graphene matrix. The obtained powder was dried overnight in oven under air atmosphere at 50 °C. The powder was then subjected to the second reduction step, consisting in a thermal annealing (temperature ramp of 1 °C min⁻¹ from T = 25 °C to T = 700 °C) in Ar:H₂ atmosphere (95:5 v/v). In this step, the oxygen functionalities of GO are severely decreased and the sp²-hybridized carbon network is restored, which is mandatory to achieve superior electrical conductivity [38,39]. Furthermore, during thermal annealing PAA acts as additional carbon source thus improving the overall conductivity. This process yields the final reduced graphene oxide/silicon nanocomposite as a greyish powder labeled Si/RGO.

2.2. Nanocomposite powder characterization

Chemical, structural and morphological characterizations of Si/RGO nanocomposite has been carried out by thermogravimetric analysis (TGA), Fourier-transform infrared spectroscopy (FTIR), X-ray diffraction (XRD), transmission electron microscopy (TEM), scanning electron microscopy (SEM). Carbonaceous matrix content has been evaluated by thermal analysis, using a Perkin–Elmer® STA6000 TGA balance under air atmosphere. FTIR measurements have been carried out using a Perkin–Elmer® Spectrum 100 FTIR Spectrometer with an ATR sample holder in the wavenumber range 4000 cm⁻¹–650 cm⁻¹. XRD patterns have been collected on a Philips diffractometer equipped with a Cu-K_α source ($\lambda = 1.504 \text{ \AA}$) and Bragg–Brentano geometry in the 5°–60° 2θ range. TEM has performed using a JEOL JEM-1010 instrumentation. SEM has been performed using a Zeiss AURIGA FIB-SEM microscope.

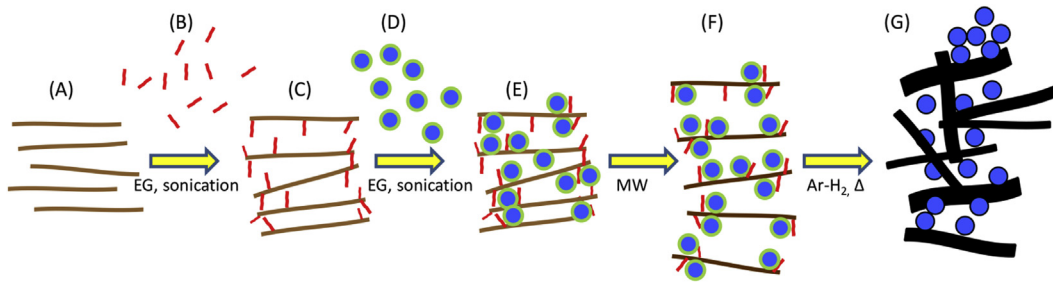


Fig. 1. Schematics of the synthetic route of the Si/RGO nanocomposite powder. (A) Graphene oxide; (B) low-molecular weight PAA; (C) PAA-functionalized GO; (D) oxide-coated Si nanoparticles; (E) Si dispersed in PAA-GO; (F) Si dispersed in partially reduced PAA-GO; (G) Si/RGO nanocomposite powder.

2.3. Electrodes preparation

Electrodes have been prepared by using high-molecular weight PAA (Sigma–Aldrich – mw = 100,000) binder dissolved in water/ethanol mixture (5:95 w/w). Si/RGO nanocomposite and SuperP conductive additive (MMM-Carbon), previously mixed and ground in an agate mortar, were added to the binder solution resulting in a slurry with a Si/RGO:SuperP:binder composition equal to 70:10:20 (mass ratio). After 4 h of stirring, the slurry was spread onto a copper foil using the ‘Doctor Blade’ technique and dried at 70 °C in air. 9 mm-diameter circular electrodes, with loadings of 1 mg cm⁻², were cut and pressed applying a specific pressure of 11 tons cm⁻².

2.4. Electrochemical measurements

Three-electrode T-shaped cells were assembled in Ar-filled glove box, using metal lithium (Sigma–Aldrich) as counter and reference electrodes. LiPF₆ 1 M in ethylene carbonate:dimethyl carbonate (EC:DMC) 1:1 w/w (LP30 by Merck) has been used as conventional electrolyte. A second type of electrolyte was prepared by adding 5% wt. of Vinylene Carbonate (VC–Sigma Aldrich) to pristine LP30.

The cells were cycled in the potential range 0.01 V–1 V with specific currents between 50 mA g⁻¹ and 500 mA g⁻¹ using a VMP-2Z multi-channel galvanostat–potentiostat (Bio-Logic, France). All

the cells were kept at open circuit potential for 24 h before starting galvanostatic cyclations, in order to allow an appropriate wetting of the electrodes. Electrochemical impedance spectroscopy (EIS) was performed applying a ±5 mV sinusoidal perturbation over the 1 V bias potential. All the measurements have been performed at $T = 20$ °C. For sake of comparison, all the specific capacity, current and resistance values are normalized to the overall Si/RGO active material mass. All potentials are given vs Li⁺/Li couple.

3. Results and discussion

3.1. Chemical, structural and morphological characterization

The structures of GO precursor, PAA-GO intermediate and Si/RGO nanocomposite have been investigated by FTIR analysis and XRD. In Fig. 2a, the FTIR spectrum of GO precursor is characterized by a wide band around 3000 cm⁻¹–3500 cm⁻¹ associated to –OH groups stretching, a double peak around 1600 cm⁻¹–1700 cm⁻¹ coming from C=O moieties, different adsorption bands between 1220 cm⁻¹ and 1100 cm⁻¹ typical of C–OH and C–O stretching, a fingerprint region below 1000 cm⁻¹ directly related to the presence of C–C bonds [33]. With respect to GO precursor, the PAA-GO FTIR spectrum (Fig. 2b) shows two additional narrow peaks around 2800 cm⁻¹–2900 cm⁻¹ that may be attributed to the aliphatic C–H moieties of PAA. Furthermore, the strong absorbance in the region

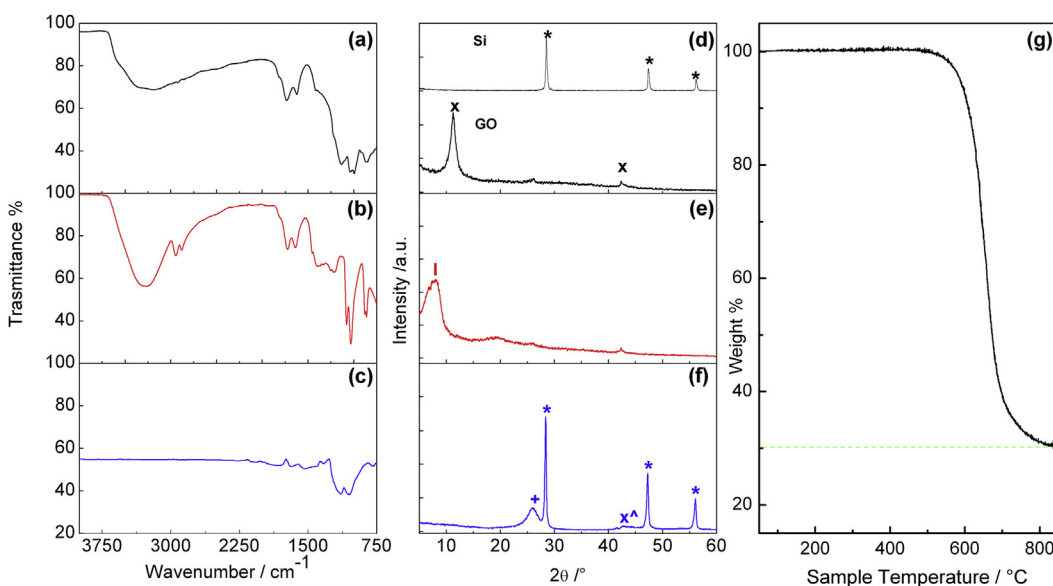


Fig. 2. FTIR spectra of: (a) GO precursor; (b) PAA-GO; (c) Si/RGO nanocomposite. XRD patterns of: (d) Si and GO precursors; (e) PAA-GO; (f) Si/RGO nanocomposite. Positions of main reflections are marked as (x) = GO; (l) = PAA-GO; (+) = RGO; (*) = Si; (^) = SiO₂. (g) TGA plot of Si/RGO nanocomposite.

1200 cm^{-1} – 1400 cm^{-1} , typical of C–O–C vibrations, indicates a successful PAA functionalization of the GO precursor. In the FTIR spectrum of Si/RGO nanocomposite (Fig. 2c) the bands related to the –OH and C=O functional groups of PAA are no longer present. The peaks between 1200 cm^{-1} and 1000 cm^{-1} appear very weak and a general decrease of the transmission signal, characteristic of an electrically conducting carbon material, can be observed [37].

Fig. 2d–f shows the diffraction patterns of pristine Si (oxide-coated), GO, PAA-GO and Si/RGO, respectively. In Fig. 2d the broad peak located around $2\theta = 11^\circ$ is typical of graphene oxide [40,41], while Si reflections are clearly visible at $2\theta = 28.4^\circ$, 47.3° and 56.1° [42]. SiO_x , if formed, is not detectable probably because of the very low amount and thickness of the oxide layer. The GO peak shifts toward lower angles in Fig. 2e, revealing an increase of the graphene interplanar distances and, hence, a successful functionalization by PAA. The diffraction pattern of the final Si/RGO nanocomposite (Fig. 2f) exhibits the peaks corresponding to Si reflections, while the broad peak centered about $2\theta = 25.5^\circ$ and the very small shoulder around $2\theta = 43^\circ$ are typical of RGO [40,41]. It should be noted that part of the signal around $2\theta = 43^\circ$ could be related to the presence of minor amounts of SiO_2 as a surface oxidation product of Si powder, either coming from pristine SiO_x coating or from handling of the Si/RGO composite under air atmosphere. However, as for pristine oxide-coated Si powder, the coating is so thin that it is hardly noticeable in the XRD pattern of the composite.

In order to evaluate Si/RGO composition, TGA was performed under air atmosphere, removing all the carbon content as CO_2 and assigning the residual weight to Si (also including minor amounts of SiO_2). As shown in Fig. 2g, the nanocomposite is stable up to $600\text{ }^\circ\text{C}$, where the weight loss through CO_2 formation initiates, resulting in a Si weight content around 31%.

Fig. 3a shows the morphology of pristine Si nanoparticles as revealed by TEM. The average Si size is in the range 50–100 nm, even if some larger aggregates exist. Fig. 3b and c shows the TEM and SEM microographies of Si/RGO nanocomposite powder. Si nanopowder, with size still in the range of 50–100 nm, appears dispersed between wrinkled RGO nanosheets, while at the same time there is evidence that a portion of Si forms larger aggregates outside the RGO matrix. RGO nanosheets exhibit a thickness that can be roughly estimated around 20 nm. Fig. 3d shows the surface

morphology of the composite electrode. A quite homogeneous distribution of the Si nanoparticles, tightly bounded to the sheets of RGO, is revealed. These results suggest that the carbonaceous matrix succeeded in retaining a stable Si dispersion after electrodes preparation.

3.2. Charge/discharge behavior in conventional $\text{LiPF}_6/\text{EC}/\text{DMC}$ electrolyte

Fig. 4a–d shows selected galvanostatic charge/discharge profiles of the Si/RGO electrode acquired at different specific currents and in the potential range $0.01\text{ V} < E < 1\text{ V}$. During the first discharge (lithiation) the capacity is 1850 mAh g^{-1} (Fig. 4a), vs a value of 1160 mAh g^{-1} for the following dealloying process, giving a first cycle columbic efficiency of about 60%. The low efficiency is associated with processes occurring at the interface between active material and electrolyte, namely the formation of a solid electrolyte interphase (SEI) taking place over an extended potential range from about 0.8 V down to about 0.2 V with an associated irreversible capacity in excess of 400 mAh g^{-1} . Further irreversible capacity may arise from Li storage at the surface, cavities and defects of disordered carbon matrix [43,44]. The sloping plateau below 0.15 V may be attributed to lithium intercalation into RGO and to formation of Li–Si alloys [27,45]. The profile of the first charge reveals two pronounced features at about 0.3 V and 0.45 V , typical of delithiation from Li–Si alloys [46]. In the subsequent cycles, two couples of reversible plateaus at about 0.25 V and 0.1 V during discharge, and at 0.3 V and 0.45 V during charge, which are respectively related to Li–Si alloying and dealloying, are evident. This is also true for the charge/discharge curves recorded at lower specific currents (Fig. 4b–d).

A clearer picture of the electrode processes can be gained from the differential capacity plots for the same cycles, shown in Fig. 5a–d. The SEI formation during the first electrode discharge is only partially visible between 0.8 V and 0.2 V because of overlapping by the high and broad irreversible peak A, corresponding to the sloping plateau in Fig. 4a. This feature is related to the first Li–Si alloying, when at room temperature the crystalline framework of Si is converted to amorphous $\alpha\text{-Li}_x\text{Si}_y$ alloys [47]. During the following charge two broad peaks, B, C at about 0.3 V and 0.45 V , and a sharp peak D at 0.43 V are present. Features B and C may be assigned to

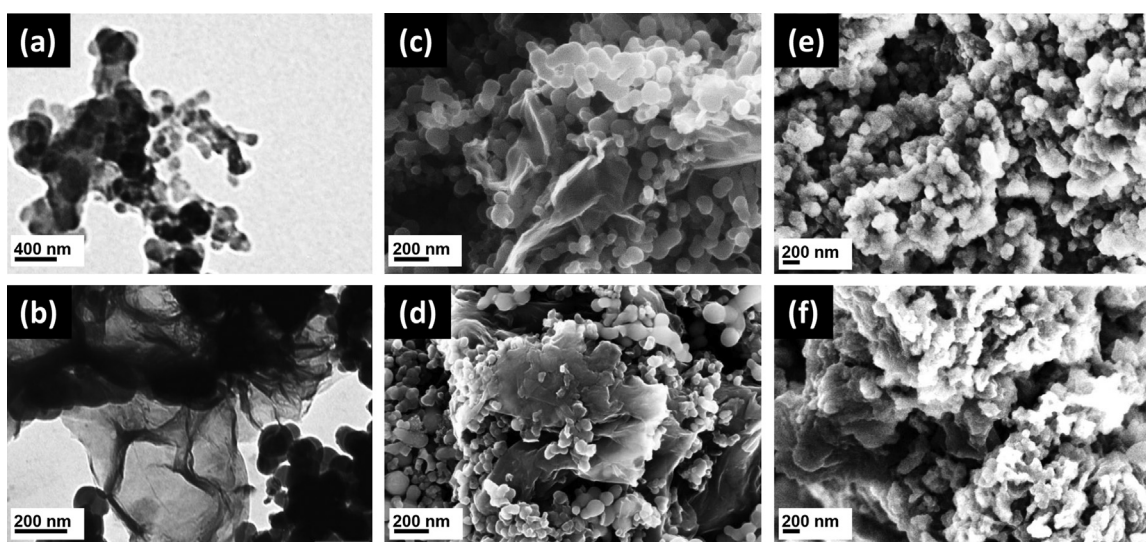


Fig. 3. TEM micrographs of: pristine Si powder (a), Si/RGO nanocomposite (b). SEM micrographs of: Si/RGO nanocomposite (c), fresh Si/RGO-based electrode (d), post-mortem Si/RGO electrodes cycled in ‘conventional’ (e) and VC-modified (f) electrolytes.

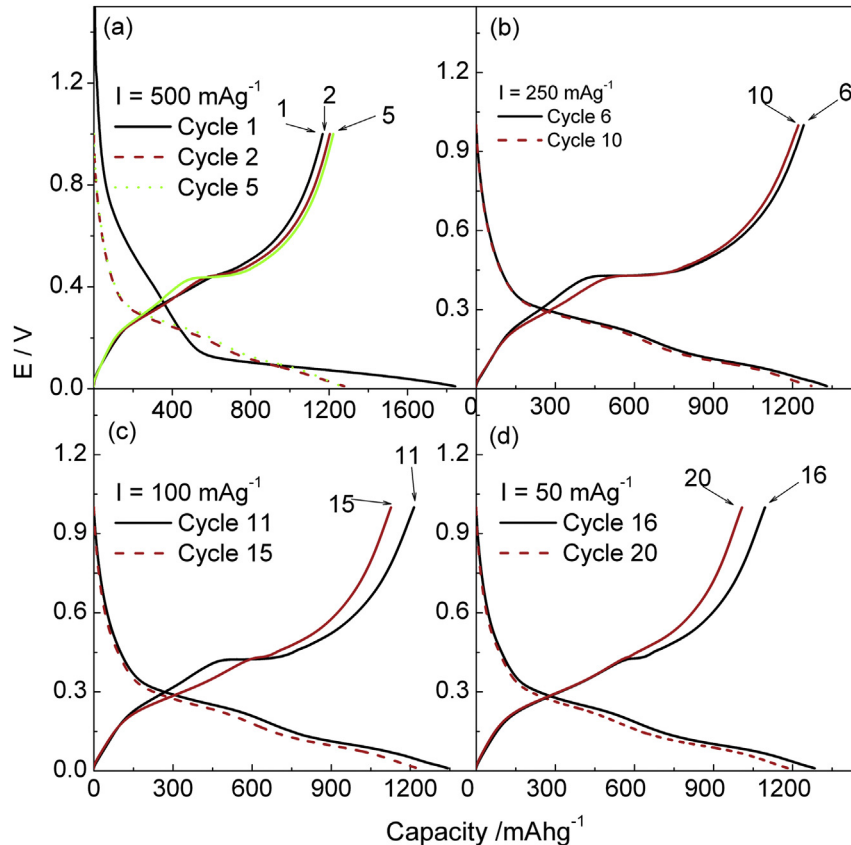


Fig. 4. Charge/discharge profiles of Si/RGO anode in LiPF_6 1 M EC:DMC 1:1 electrolyte. $T = 20^\circ\text{C}$. $0.01 \text{ V} < E < 1 \text{ V}$. Specific currents applied: 500 mA g^{-1} (a), 250 mA g^{-1} (b), 100 mA g^{-1} (c) and 50 mA g^{-1} (d). Cycle numbers are shown in the plot.

single-phase dealloying from amorphous $\text{a-Li}_x\text{Si}_y$, while peak D describes a sharp two-phase transition. This implies that during the first Li alloying the amorphous $\text{a-Li}_x\text{Si}_y$ partially converts, in the potential range 50 mV–70 mV, into a new crystalline phase that has been identified as $\text{Li}_{15}\text{Si}_4$ by Obrovach and Christensen [45]. During the following dealloying, the crystalline phase converts to amorphous a-Si at about 0.43 V (peak D). Further support for this interpretation comes from the profiles related to the following cycles, where the small peak G and the coupled peak D indicate the formation and the dissolution of the crystalline phase $\text{Li}_{15}\text{Si}_4$, while the broad peaks E and F, coupled with peaks B and C, describe alloying/dealloying of amorphous silicon. The reversibility of the broad peaks (E, F, B, C) during lithiation and delithiation, suggest that, after first lithiation, most of the capacity of the composite anodes is exchanged by amorphous a-Si and $\text{a-Li}_x\text{Si}_y$, while only minor amounts involve the crystalline $\text{Li}_{15}\text{Si}_4$ (peaks G, D). Peak D is progressively higher and sharper going from cycle 1 to cycle 5 at 500 mA g^{-1} (Fig. 5a), while an opposite trend is found in the curves recorded at the lower specific currents (Fig. 5b–d). This behavior suggests that the crystalline phase formation depends on cycling conditions and ‘history’ of the electrode, and is consistent with the evolution of capacity values shown in Fig. 6. The capacity increases from cycle 1 to cycle 5, because of progressive electrode wetting and activation, that increase the Si utilization and, hence, the amount of crystalline phase formed. Given the $\text{Li}_{15}\text{Si}_4$ stoichiometry for the fully lithiated alloy that limits the Si theoretical reversible capacity to 3579 mAh g^{-1} , the maximum contribution to capacity coming from Si in the composite is 1110 mAh g^{-1} . Thus, the additional anode capacity is provided, at least during the initial cycles, by the RGO matrix via reversible Li intercalation between the

planes of carbon and storage at the surface of its defects or pores [42,48,49]. The carbon contribution to capacity is compatible with the values, ranging approximately between 150 mAh g^{-1} and 350 mAh g^{-1} , commonly found for amorphous carbon matrixes [49].

After the activation cycles, the formation of the crystalline Li–Si end-member is progressively hindered as electrode cycling proceeds, as confirmed by the fading and shifts of peaks D, G in Fig. 5b–d and by the capacity decay in Fig. 6. A likely explanation of these two concurrent phenomena may be found considering several factors, such as contact with current collector, charge/discharge currents and, mainly, the active material size and morphology, that could impact on crystallization of $\text{a-Li}_x\text{Si}_y$ to $\text{Li}_{15}\text{Si}_4$. In fact, it is known that Li alloying and dealloying through amorphous phases are preferred for smaller Si size, while the formation of the crystalline phase is promoted as the Si size increases [19]. This is likely to occur during the ‘activation’ cycles when larger Si aggregates, not efficiently embedded into the RGO matrix (see Fig. 3a), may tend to further aggregation as a consequence of large volume changes at high-Li content [50,51], thus favoring formation of crystalline $\text{Li}_{15}\text{Si}_4$. However, this causes mechanical stress, cracking, and loss of contact of some portions of active material [19–21], resulting in the progressive disappear of the crystalline phase.

This interpretation is further supported by the stability tests (Fig. 7) in which the capacity retention has been evaluated by means of 100 charge/discharge cycles at a specific current of 500 mA g^{-1} (EIS measurements have been performed after every 5th cycle in order to monitor the cell polarizations). As shown in Fig. 7a, during the electrode ‘activation’ cycles, the specific

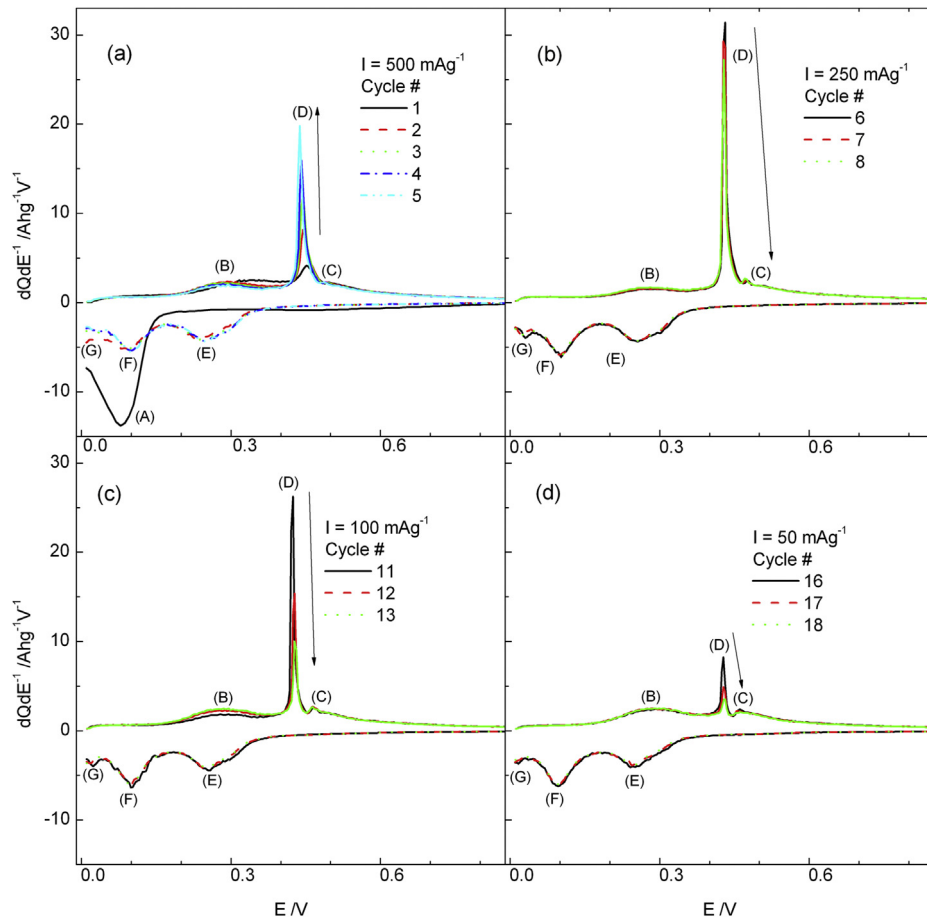


Fig. 5. Calculated $dQdE^{-1}$ vs E differential profiles of Si/RGO anode in LiPF_6 1 M EC:DMC 1:1 electrolyte. $T = 20^\circ\text{C}$. $0.01 \text{ V} < E < 1 \text{ V}$. Specific currents applied: 500 mA g^{-1} (a), 250 mA g^{-1} (b), 100 mA g^{-1} (c), 50 mA g^{-1} (d). Cycle numbers are shown in the plot.

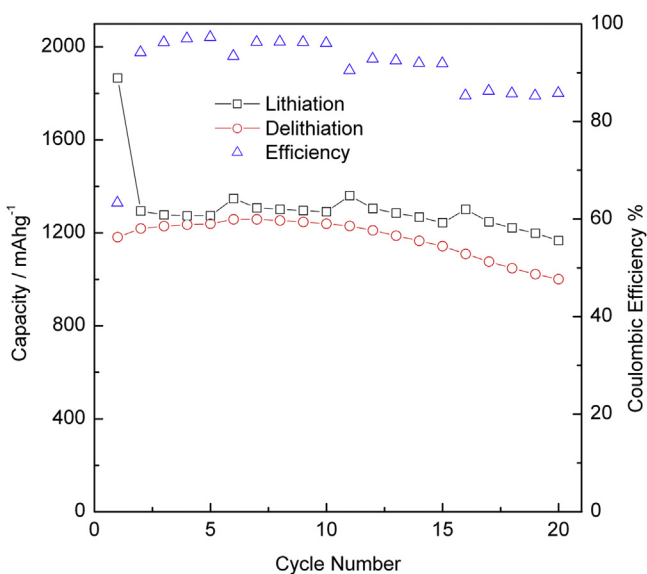


Fig. 6. Charge/discharge capacities and Coulombic efficiency of Si/RGO anode in LiPF_6 1 M EC:DMC 1:1 electrolyte. $T = 20^\circ\text{C}$. $0.01 \text{ V} < E < 1 \text{ V}$. Specific currents applied: 500 mA g^{-1} (cycles 1–5), 250 mA g^{-1} (cycles 6–10), 100 mA g^{-1} (cycles 11–15), 50 mA g^{-1} (cycles 16–20).

dealloying capacity raises from 1050 mAh g^{-1} to 1150 mAh g^{-1} . At the same time, in Fig. 7b peaks at 0.025 V (during Li uptake) and 0.43 V (during Li release) confirm the involvement of increasing amounts of the crystalline end-member $\text{Li}_{15}\text{Si}_4$ in the charge/discharge processes. After these ‘activation’ cycles, as a consequence of the mechanical stress induced by the crystalline phase, the reversibility of $\text{Li}_{15}\text{Si}_4$ formation and more generally of the electrode is compromised, as enlightened by the progressive fade of the delithiation peak at 0.43 V (Fig. 7c and d). This results in a rapid capacity decay that leads to residual capacity values of 330 mAh g^{-1} after 100 cycles, corresponding to about 30% of the initial capacity. Post-mortem SEM micrograph (Fig. 3e) of the electrode after 100 cycles clearly shows aggregation of the silicon nanoparticles on the surface of the electrode when compared to the micrograph of the un-cycled electrode in Fig. 3d.

3.3. Charge/discharge behavior in modified $\text{LiPF}_6/\text{VC}/\text{EC}/\text{DMC}$ electrolyte

The charge/discharge properties and the capacity retention of Si/RGO composite anodes greatly improve when the electrode is cycled in LP30 electrolyte modified by addition of Vinylene Carbonate (VC) (VC:LP30 5:95 mass ratio). VC is a member of the so called ‘reaction-type additives’ that, during the first discharge, undergoes a reductive polymerization at potentials slightly more positive than those of the SEI formation ($\sim 0.8 \text{ V}$) [52]. As a consequence, a polymerized VC film is initially formed on the carbon

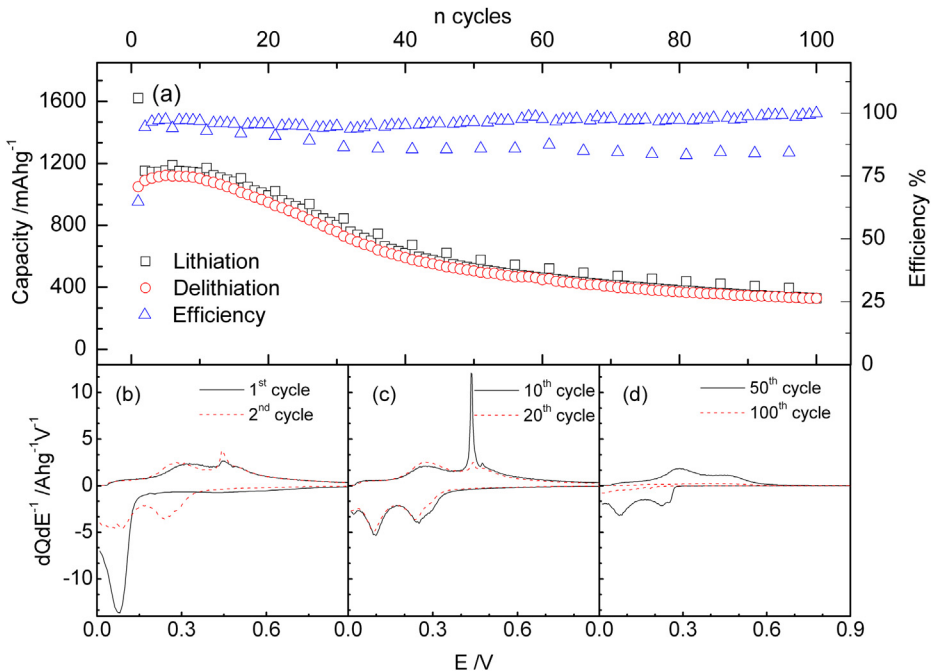


Fig. 7. Capacity retention test of Si/RGO anode in LiPF_6 1 M EC:DMC 1:1 electrolyte. $T = 20^\circ\text{C}$. $0.01 \text{ V} < E < 1 \text{ V}$. Specific current = 500 mA g^{-1} . Charge/discharge capacities and Coulombic efficiency (a). Calculated dQ/dE^{-1} vs E differential profiles for cycles 1, 2 (b), 10, 20 (c), 50, 100 (d).

surface. When the potential is further lowered, this layer modulates the catalytic activity of the carbon toward EC and DMC decomposition and promotes the formation of a more homogeneous and stable SEI [53].

Fig. 8 shows some selected charge/discharge profiles at different specific currents (panels a, b) and the corresponding differential capacity profiles (panels c, d). The curves closely resemble those obtained in the VC-free electrolyte. The discharge capacity during

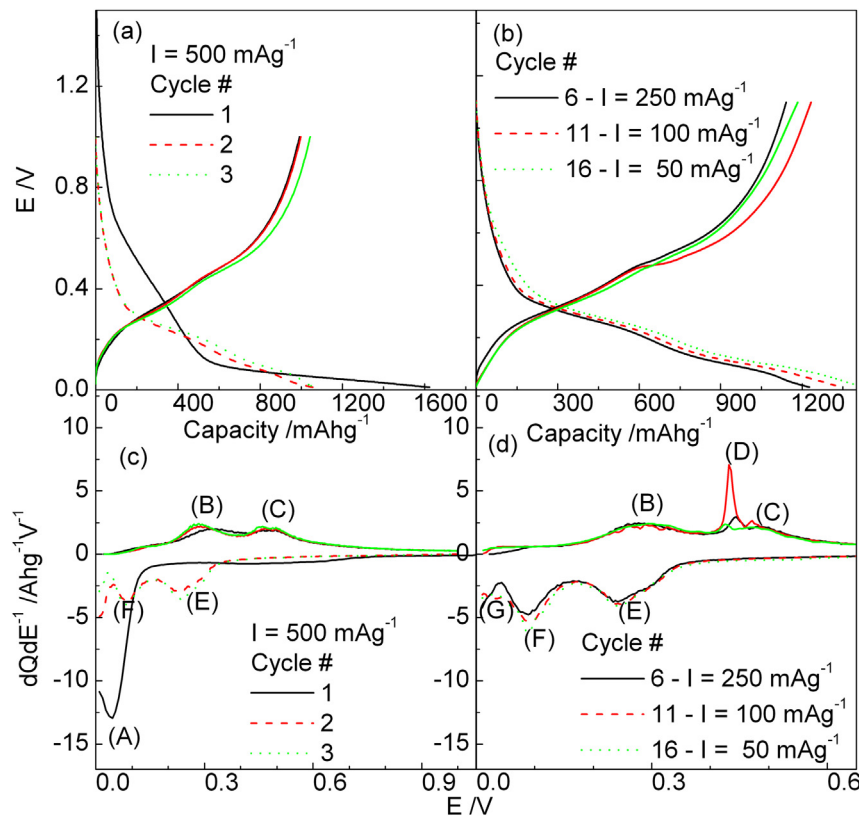


Fig. 8. Charge/discharge profiles (a, b) and corresponding dQ/dE^{-1} vs E differential profiles (c, d) of Si/RGO anode in 5% VC-modified LiPF_6 1 M EC:DMC 1:1 electrolyte. $T = 20^\circ\text{C}$. Specific currents applied: 500 mA g^{-1} , 250 mA g^{-1} , 100 mA g^{-1} , 50 mA g^{-1} .

the first cycle (Fig. 8a) run at a specific current of 500 mA g⁻¹ is about 1624 mAh g⁻¹, with an irreversible capacity close to 640 mAh g⁻¹, corresponding to formation of SEI over a potential range from about 0.8 V to about 0.2 V. The extended sloping plateau at potentials lower than 0.2 V is quite similar to that found in LP30 electrolyte and consistently appears in the first differential profile (Fig. 8c) as the high peak A. The differential curves related to the first charge and to the following charge/discharge cycles exhibit the couples of peaks E, F and B, C characteristic of formation and dissolution of amorphous Li–Si alloys. No evidences for the sharp peak D and the corresponding peak G, characteristic of crystalline Li₁₅Si₄, are seen at 500 mA g⁻¹. Peaks D, G appear only when the specific currents are lower (Fig. 8d), implying decreased polarization and favorable conditions for the formation of the crystalline end-member. The beneficial effect of VC on the stability of the electrode clearly results from the capacity retention plots in Fig. 9a where the discharge capacity, after an increase from the initial value of 1050 mAh g⁻¹ to 1120 mAh g⁻¹ during activation cycles, decays to 815 mAh g⁻¹ after 100 cycles, vs a final value of 320 mAh g⁻¹ for the electrode in the VC-free electrolyte. The reason of this increased stability is again to be found in the very limited formation of the crystalline Li₁₅Si₄ phase, as results from the differential capacity plots in Fig. 9b–d, where there is no evidence of the sharp peak at 0.43 V. This behavior confirms that the formation of the crystalline Li₁₅Si₄ phase is one of the main reasons, if not the most important, of capacity fade and failure of Li–Si alloy anodes. The relative stability of the Si/RGO electrodes in VC-containing electrolyte is also evidenced from the comparison of the *post-mortem* SEM micrographs (Fig. 3e and f) of the electrodes recorded after 100 cycles in both electrolytes. The Si particles are still small and with a well-defined morphology for the electrode cycled in the VC-containing electrolyte (Fig. 3f), in comparison with those cycled in the VC-free solvent (Fig. 3e). The RGO layers, in addition, are still visible in Fig. 3f, confirming the effectiveness of VC in preserving the electrode morphology.

3.4. Electrochemical impedance spectroscopy characterization

The ac-impedance spectra recorded at cycles 5, 15, 25 and 50 in both electrolytes during the capacity retention tests are shown in Fig. 10a–d. All the Nyquist plots show common features: two semicircles partly overlapped, especially for the VC-containing cell, at high-to-medium frequencies, followed by a sloping line in the low-frequency region. These features, typical of Li-ion intercalation or alloying anodes [49,54], can be assigned, from higher to lower frequencies, to: (i) impedance of SEI at electrode/electrolyte interface, (ii) charge-transfer resistance coupled with double layer capacitance, (iii) diffusion to a blocking electrode. During the initial cycles (panel a) the overall impedance of the cell containing the VC-modified electrolyte is higher than that of the cell containing the conventional one. With increasing number of cycles, the impedance of the cell with conventional electrolyte dramatically increases, while that of the cell with VC remains stable. After 15 cycles the low-frequency responses of both cells become comparable (panel b). After 25 cycles (panel c), the overall impedance of the cell containing the conventional electrolyte is higher, while contributions in the medium-to-high frequency region (see inset) are similar. Finally, after 50 cycles (panel d), the impedance of the cell with the VC-modified electrolyte is much lower both at high and at low frequencies. From these findings, the impact of VC addition on the passivation layer behavior is clear. The addition of an intermediate layer, made of VC polymerization products, between carbon surface and ‘classical’ SEI, initially results in an increased high-frequency impedance (inset in Fig. 10a), which is due to Li⁺ migration through a thicker interphase. However, the VC-modified SEI results more stable. In fact, with increasing number of cycles, the high-frequency semicircle remains practically constant in presence of VC, while it grows at least of one order of magnitude in the other case.

All the Nyquist plots have been analyzed by the equivalent circuit method using Boukamp's Equivalent Circuit software [55]. The

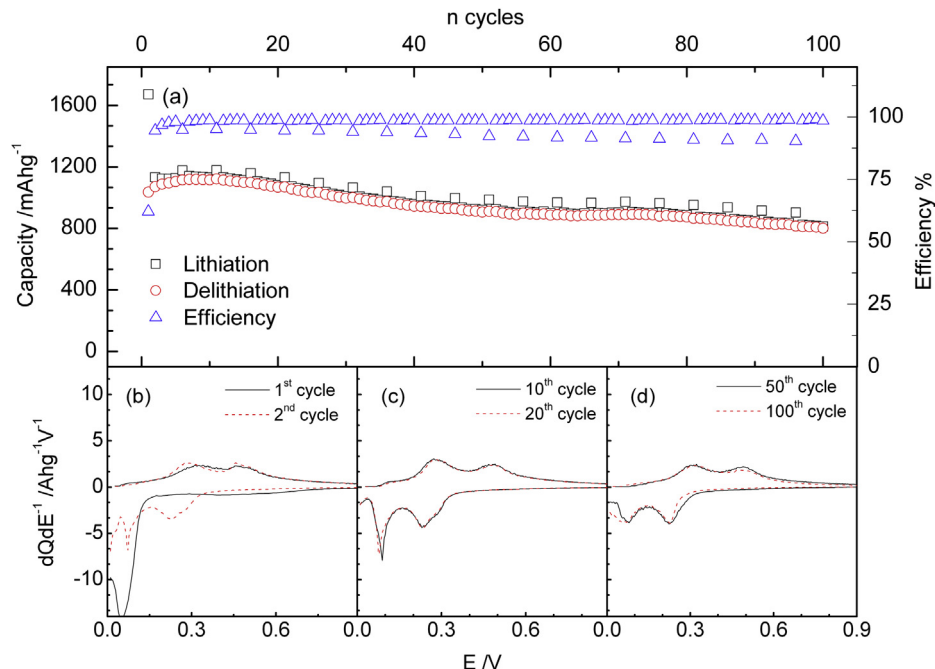


Fig. 9. Capacity retention test of Si/RGO anode in 5% VC-modified LiPF₆ 1 M EC:DMC 1:1 electrolyte. T = 20 °C. 0.01 V < E < 1 V. Specific current = 500 mA g⁻¹. Charge/discharge capacities and Coulombic efficiency (a). Calculated dQdE⁻¹ vs E differential profiles for cycles 1, 2 (b), 10, 20 (c), 50, 100 (d).

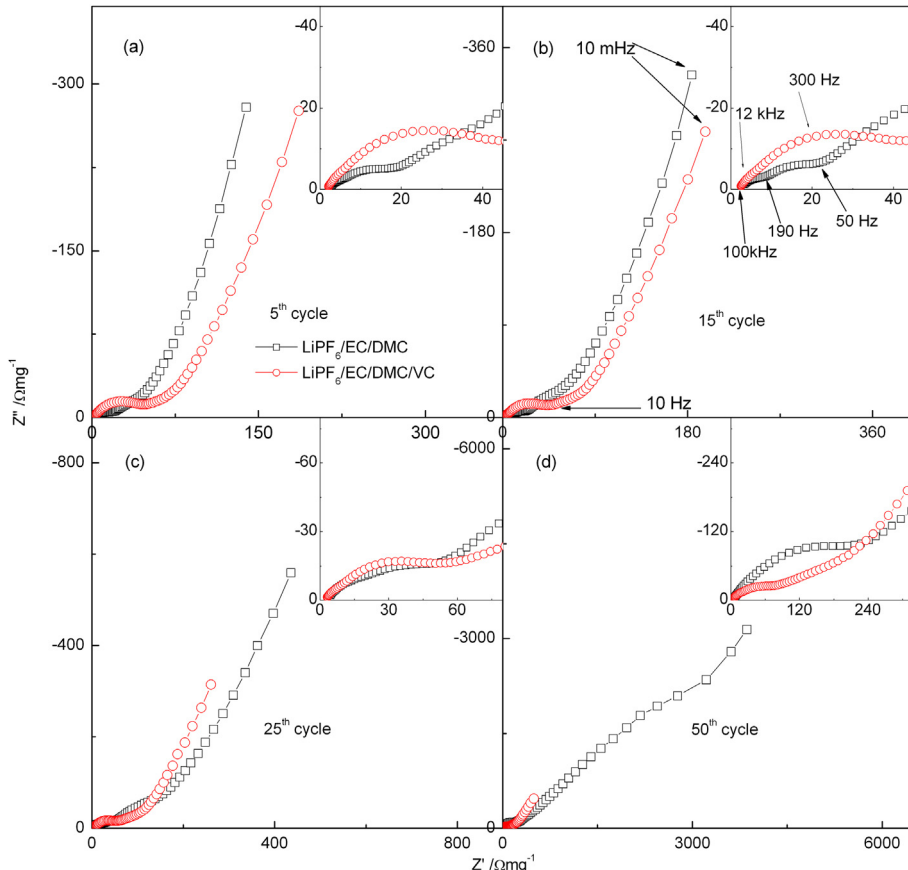


Fig. 10. Nyquist plots of Si/RGO anode in pristine (□) and 5% VC-modified (○) LiPF₆ 1 M EC:DMC 1:1 electrolytes after 5 (a), 15 (b), 25 (c), 50 (d) cycles at $I = 500 \text{ mA g}^{-1}$. $T = 20^\circ\text{C}$. $E = 1 \text{ V}$. $1 \text{ mHz} < f < 100 \text{ kHz}$. The insets detail the high-frequency region. Characteristic frequencies are shown in panel (b).

impedance dispersions have been fitted to a circuit $R_{\text{el}}(R_{\text{SEI}}C_{\text{SEI}})(R_{\text{ct}}C_{\text{dl}})WC_i$, according to Boukamp's notation, where R_{el} , R_{SEI} , R_{ct} are the resistances associated with electrolyte, passivation layer and charge-transfer process, respectively, C_{SEI} , C_{dl} are the capacitances associated to passivation layer and electric double layer, W is the diffusive Warburg impedance, C_i is the differential intercalation capacity. In the fitting procedure, all the C and W elements have been substituted by constant phase elements Q , in order to take into account the deviations from ideality coming from electrodes inhomogeneities and roughness [56]. The trends of the calculated SEI resistances are shown in Fig. 11. For the VC-containing cell the R_{SEI} value, initially higher ($20 \Omega \text{ mg}^{-1}$ vs $4 \Omega \text{ mg}^{-1}$), increases to $50\text{--}60 \Omega \text{ mg}^{-1}$ after 100 cycles, while that in conventional LP30 electrolyte reaches a value of $200 \Omega \text{ mg}^{-1}$ after the same number of cycles. This confirms the relevant VC contribution to formation and stabilization of the passivation layer. In addition, it should be noted that the initially higher impedance reflects a higher polarization of the VC-containing cell, which may contribute in hampering the formation of the crystalline Li₁₅Si₄ phase, resulting in better mechanical stability, also at low potentials, and in a highly improved charge/discharge reversibility.

4. Conclusions

A facile and inexpensive synthesis for a high-performance graphene/silicon nanocomposite, which can be used as lithium-ion battery anode material, has been demonstrated. Use of low-molecular weight PAA-functionalized graphene oxide in the first stage of the synthesis successfully avoided the complete re-stacking of graphene layers and improved the dispersion of Si

nano-particles in the carbonaceous matrix. A two-step reduction process allowed to obtain a Si/RGO nanocomposite with suitable composition, morphology and structure. A relatively green approach has been used in the preparation of electrodes, using

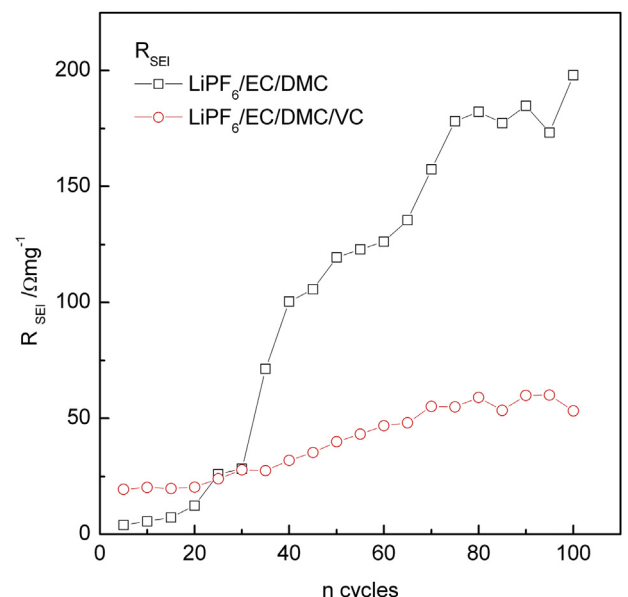


Fig. 11. Values of the calculated resistance of the passivation layer (R_{SEI}) for Si/RGO anode in pristine (□) and 5% VC-modified (○) LiPF₆ 1 M EC:DMC 1:1 electrolytes.

high-molecular weight PAA dissolved in ethanol, which allowed optimization of electrode morphology.

Electrochemical properties of the nanocomposite anode were evaluated in terms of rate capability and capacity retention. The electrodes showed specific capacity values of the order of 1000 mAh g⁻¹ and good reversible behavior, especially at relatively high specific current values. The poor capacity retention in conventional LiPF₆/EC/DMC has been dramatically improved by the addition of vinylene carbonate to the electrolyte blend. Specific capacity of more than 800 mAh g⁻¹ after 100 cycles at 500 mA g⁻¹ specific current has been reached.

The differential analysis of the galvanostatic profiles showed that most of capacity is exchanged by Li–Si reversible alloying mechanisms which involve amorphous phases. The formation of the crystalline Li₁₅Si₄ end-member, promoted at low current and polarization, has been revealed as the main threat to the stability of the anode and to the reversibility of the charge/discharge processes. Furthermore, RGO matrix has been demonstrated to contribute as electroactive material in increasing the overall electrode capacity. The electrochemical impedance spectroscopy measurements confirmed a crucial role of VC addition in the formation of a stable passivation layer.

These results clearly demonstrate that the use of PAA-based polymers, both for GO functionalization and as electrode binder, together with VC as electrolyte additive, concur in stabilizing the electrode morphology and in enhancing the electrochemical performances of the Si/RGO nanocomposite, which can thus act as a very stable, high-capacity anode material for Li-ion batteries.

Acknowledgments

This research is funded by ENEA and Ministero dello Sviluppo Economico Italiano within the project “Ricerca di materiali anodici per batterie litio ione operanti in elettroliti organici convenzionali di più elevata energia rispetto a quelle sul mercato”. The authors want to thank Dr. Claudia Ramírez-Castro at the Westfälische Wilhelms-Universität Münster for her support in recording SEM micrographs at MEET (Münster Electrochemical Energy Technology).

References

- [1] K. Mizushima, P.C. Jones, P.J. Wiseman, J.B. Goodenough, Solid State Ionics 3 (1981) 171.
- [2] M.G.S.R. Thomas, P.G. Bruce, J.B. Goodenough, Solid State Ionics 17 (1985) 13.
- [3] Y. Nishi, J. Power Sources 100 (2001) 101.
- [4] V. Etacheri, R. Marom, R. Elazari, G. Salitra, D. Aurbach, Energy Environ. Sci. 4 (2011) 3243.
- [5] J.W. Fergus, J. Power Sources 195 (2010) 939.
- [6] B. Ellis, K.T. Lee, L.F. Nazar, Chem. Mater. 22 (2010) 691.
- [7] M. Hu, X. Pang, Z. Zhou, J. Power Sources 237 (2013) 229.
- [8] M. Park, X. Zhang, M. Chung, G.B. Less, A.M. Sastry, J. Power Sources 195 (2010) 7904.
- [9] Y.P. Wu, E. Rahm, R. Holze, J. Power Sources 114 (2003) 228.
- [10] M. Winter, K.-C. Moeller, J.O. Besenhard, in: G.-A. Nazri, G. Pistoia (Eds.), *Lithium Batteries. Science and Technology*, Springer, New York, 2003, pp. 144–195.
- [11] M.B. Armand, D.W. Murphy, in: J. Broadhead, B.C. Steele (Eds.), *Material for Advanced Batteries*, Plenum Press, New York, 1980, p. 145.
- [12] Y. Wu, J. Power Sources 111 (2002) 329.
- [13] B. Scrosati, J. Garche, J. Power Sources 195 (2010) 2419.
- [14] K. Zaghib, M. Simoneau, M. Armand, M. Gauthier, J. Power Sources 81–82 (1999) 300.
- [15] D.A.C. Brownson, D.K. Kampouris, C.E. Banks, J. Power Sources 196 (2011) 4873.
- [16] W.J. Zhang, J. Power Sources 196 (2011) 13.
- [17] R.A. Huggins, Solid State Ionics 113–115 (1998) 57.
- [18] J. Li, J.R. Dahn, J. Electrochem. Soc. 154 (2007) A156.
- [19] T.D. Hatchard, J.R. Dahn, J. Electrochem. Soc. 151 (2004) A838.
- [20] M. Winter, J.O. Besenhard, Electrochim. Acta 45 (1999) 31.
- [21] Z. Chen, V. Chevrier, L. Christensen, J.R. Dahn, Electrochim. Solid State Lett. 7 (2004) A310.
- [22] M.T. McDowell, W.L. Seok, I.I. Ryu, W. Hui, W.D. Nix, J.W. Choi, Y. Cui, Nano Lett. 11 (2011) 4018.
- [23] M. Holzapfel, H. Buqa, F. Krumeich, P. Novák, F.-M. Petrat, C. Veit, Electrochim. Solid State Lett. 8 (2005) A516.
- [24] T.H. Hwang, M.L. Yong, B.-S. Kong, J.-S. Seo, J.W. Choi, Nano Lett. 12 (2012) 802.
- [25] X. Li, P. Meduri, X. Chen, W. Qi, M.H. Engelhard, W. Xu, F. Ding, J. Xiao, W. Wang, C. Wang, J.-G. Zhang, J. Liu, J. Mater. Chem. 22 (2012) 11014.
- [26] Z.-S. Wu, G. Zhou, L.-C. Yin, W. Ren, F. Li, H.-M. Cheng, Nano Energy 1 (2012) 107.
- [27] J.-G. Ren, Q.-H. Wu, G. Hong, W.-J. Zhang, H. Wu, K. Amine, J. Yang, S.-T. Lee, Energy Technol. 1 (2013) 77.
- [28] H. Xiang, K. Zhang, G. Ji, J.Y. Lee, C. Zou, X. Chen, J. Wu, Carbon 49 (2011) 1787.
- [29] G. Zhou, D.-W. Wang, F. Li, L. Zhang, N. Li, Z.-S. Wu, L. Wen, G.Q. Lu, H.-M. Cheng, Chem. Mater. 22 (2010) 5306.
- [30] Y. Sun, Q. Wu, G. Shi, Energy Environ. Sci. 4 (2011) 1113.
- [31] A. Magasinski, B. Zdyrko, I. Kovalenko, B. Hertzberg, R. Burtovy, C.F. Huebner, T.F. Fuller, I. Luzinov, G. Yushin, ACS Appl. Mater. Interfaces 2 (2010) 3004.
- [32] S. Komaba, K. Shimomura, N. Yabuuchi, T. Ozeki, H. Yui, K. Konno, J. Phys. Chem. C 115 (2011) 13487.
- [33] J.I. Paredes, S. Villar-Rodil, A. Martínez-Alonso, J.M.D. Tascón, Langmuir 24 (2008) 10560.
- [34] P. Wang, Y. Zhai, D. Wang, S. Dong, Nanoscale 3 (2011) 1640.
- [35] J.K. Lee, K.B. Smith, C.M. Hayner, H.H. Kung, Chem. Commun. 46 (2010) 2025.
- [36] X. Liu, L. Pan, G. Zhu, T. Lu, Z. Sun, C. Sun, RSC Adv. 1 (2011) 1245.
- [37] H. Wu, B. Tang, P. Wu, J. Membr. Sci. 451 (2014) 94.
- [38] D.R. Dreyer, S. Park, C.W. Bielawski, R.S. Ruoff, Chem. Soc. Rev. 39 (2010) 228.
- [39] X. Zhou, Y.-X. Yin, L.-J. Wan, Y.-G. Guo, Chem. Commun. 48 (2012) 2198.
- [40] L.J. Cote, R. Cruz-Silva, J. Huang, J. Am. Chem. Soc. 131 (2009) 11027.
- [41] C. Fu, G. Zhao, H. Zhang, S. Li, Int. J. Electrochim. Sci. 8 (2013) 6269.
- [42] M. Yamada, A. Ueda, K. Matsumoto, T. Ohzuku, J. Electrochim. Soc. 158 (2011) A417.
- [43] N.A. Kaskhedikar, J. Maier, Adv. Mater. 21 (2009) 2664.
- [44] T. Zheng, W.R. McKinnon, J.R. Dahn, J. Electrochim. Soc. 143 (1996) 2137.
- [45] M.N. Obrovac, L. Christensen, Electrochim. Solid State Lett. 7 (2004) A93.
- [46] W. Wang, P.N. Kumta, ACS Nano 4 (2010) 2233.
- [47] P. Limthongkul, Y.-I. Jang, N.J. Dudney, Y.-M. Chiang, Acta Mater. 51 (2013) 1103.
- [48] J.R. Dahn, T. Zheng, Y. Liu, J.S. Xue, Science 270 (1995) 590.
- [49] F. Nobili, I. Meschini, M. Mancini, R. Tossici, R. Marassi, F. Croce, Electrochim. Acta 107 (2013) 85.
- [50] N.-S. Choi, K.H. Yew, K.Y. Lee, M. Sung, H. Kim, S.-S. Kim, J. Power Sources 161 (2006) 1254.
- [51] Y. Liu, K. Hanai, N. Imanishi, A. Hirano, Y. Takeda, Solid State Ionics 168 (2004) 61.
- [52] S.S. Zhang, J. Power Sources 162 (2006) 1379.
- [53] E. Peled, D.B. Tow, A. Merson, A. Gladkich, L. Burstein, D. Golodnitsky, J. Power Sources 97–98 (2001) 52.
- [54] F. Nobili, M. Mancini, P.E. Stallworth, F. Croce, S.G. Greenbaum, R. Marassi, J. Power Sources 198 (2012) 243.
- [55] B.A. Boukamp, Solid State Ionics 20 (1986) 31.
- [56] E. Barsoukov, J. Ross Macdonald, in: *Impedance Spectroscopy: Theory, Experiments and Applications*, second ed., John Wiley & Sons, New York, 2005, p. 83.